MICHIGAN STATE
UNIVERSITY

National Superconducting Cyclotron Laboratory

CONVERSION OF 92 MeV/u ^{38}Ca/^{37}K PROJECTILE FRAGMENTS INTO THERMALIZED ION BEAMS

Accepted for publication in Nucl. Instr. and Meth. A

L. WEISSMAN, D.J. MORRISSEY, G. BOLLEN, D.A. DAVIES, E. KWAN, P.A. LOFY, P. SCHURY, S. SCHWARZ, C. SUMITHRARACHCHI, T. SUN, R. RINGLE

MSUCL-1291 **OCTOBER 2004**

Conversion of 92 MeV/u $^{38}Ca/^{37}K$ projectile fragments into thermalized ion beams

L. Weissman[1*], D.J. Morrissey[1,2], G. Bollen[1,3], D.A. Davies[1,2], E. Kwan[1,2], P.A. Lofy[1,2], P. Schury[1,3], S. Schwarz[1], C. Sumithrarachchi [1,2], T. Sun[1,3], R. Ringle[1,3]

1. National Superconducting Cyclotron Laboratory,

2. Department of Chemistry, Michigan State University, and

3. Department of Physics and Astronomy,

Michigan State University, East Lansing, MI-48824

(Dated: October 18, 2004)

Abstract

The results of tests for stopping and extraction of energetic, 92 MeV/u, short-lived ^{38}Ca and ^{37}K fragments of 0.5% and 0.1% full width of momentum spread with the first version of the NSCL gas cell are reported. The projectile fragments were thermalized in 51 cm of helium at one bar and were transported by electric fields and gas flow into an expansion chamber through a supersonic nozzle, guided by an radio frequency quadrupole (rfq) guide and collected on a metallic wire. The extraction efficiency was measured for different implantation rates, different electrical field distributions inside the gas cell, and different values of beam degrader thicknesses. The extraction measurements were compared with the experimental stopping efficiency and measurement of ionization induced in the helium gas. Mechanisms responsible for ion losses were identified and possible improvements of the gas cell performance were discussed.

PACS numbers: 29.90+r

Keywords: gas cell, stopping relativistic fragments, extraction of ions from helium

* corresponding author: weissman@nscl.msu.edu

I. INTRODUCTION

Collection of fast secondary beams after thermalization in a high purity helium gas will allow for a new range of experiments at existing projectile fragmentation facilities and will be an important part of the next generation radioactive beam facilities [1–3]. At present, several groups around the world are working on projects to stop fast ion beams in gas catchers [4–6]. A gas stopping cell has been built at the National Superconducting Cyclotron Laboratory and will act as the first stage of the Low Energy Beam and Ion Trap (LEBIT) project [7]. The concept of the NSCL stopping cell includes careful energy degradation of fragmentation beams, with stopping and thermalization of fragments in a 51 cm long gas cell filled with high-purity helium at 1 bar pressure. A large fraction of ions is expected to remain in the 1^+ charge state in ultra pure helium. The stopped ions are drifted by electrical fields towards a supersonic nozzle and are jetted into an expansion chamber. Ions in the jet are caught by an rfq ion-guide system and delivered for low-energy experiments.

The conversion of relativistic fragments into low-energy exotic beams with a gas stopper is a challenging task. The efficient stopping of fragmentation beams with large momentum distributions in a thin gas target requires precisely machined high-quality degraders together with ion-optical compression of the beam momentum distribution. Various processes in the gas cell, such as space-charge effects, fast ion chemistry, ion recombination, and others have to be controlled in order to minimize the loss of the stopped ions. In view of the short half-lives and low production rates of the most interesting rare isotopes, a fast extraction is required.

A number of studies of stopping energetic fragments in the NSCL gas cell have been completed in which the stopping efficiency of the gas cell was measured for a number of primary and secondary beams as a function of degrader thickness, gas pressure, and path length in helium [8]. Range compression of the fragmentation beams as described in [9–11] was also tested in the NSCL system [12]. A typical stopping efficiency obtained for the beams with narrow momentum distribution was of the order of 50% [8]. A stopping efficiency of 30% was obtained for a secondary beam with a broad momentum spread utilizing the range compression method [12]. A brief report on the results from the first ion-extraction tests was presented in [13]. In this publication we report and discuss in detail the results of recent extraction tests.

II. EXPERIMENTAL SETUP

Fragmentation beams obtained from the A1900 fragment separator [14] are sent to the experimental setup. A schematic diagram of the experimental setup is presented in Fig. 1. A detailed description of the experimental setup for the range measurements can be found in earlier publications [8, 12, 13], so only a brief description of this part of the experiment is provided here. A variety of degraders including a wedge can be introduced at the dispersive focus near the gas cell for slowing down of beams. A wedge degrader at the dispersive image followed by a quadrupole doublet allows for compression of the energy spread of the fragmentation beam [10]. A large area (5x5 cm^2) telescope that consists of a 500 micron thick PIN detector and a 300 thick micron quadrant detector is positioned 86 cm upstream of the 51 cm long gas cell, and can be inserted. A 300 micron thick, 300 mm^2 active area, bakeable silicon detector can be inserted in the path of the beam inside the gas cell at a distance of 39 cm from the 1022(2) μm thick beryllium entrance window. The detector is used for particle identification using time-of-flight (TOF) and energy-loss data during the range measurements and optimization of the glass degrader thickness.

After the range measurements, the Si detector is rotated out of the beam axis in order to perform the extraction measurements. The stopped ions are drifted by an electric field created by DC voltages. A set of 21 ring electrodes provides a drifting potential along the cell axis and four concentric spherical electrodes focus the ions at the exit nozzle (Fig. 1,2a). The voltage of the first ring, at a distance of 6.5 cm from the beryllium window held at ground potential, is provided by a separate power supply. The remaining rings are connected in a chain using 1 MΩ resistors rated for high-vacuum applications and their voltages are provided by four power supplies. The nozzle is made from high-resistivity silicon that allowed one to have a voltage drop of up to 70 V along its length. The upstream side of the nozzle is in contact with the smallest spherical electrode and voltage on the exit side is varied during the tests. The potential along the gas cell length varies from the maximum voltage on the first ring (up to 2.5 kV) down to the potential on the downstream side of the nozzle (near zero). The voltage distribution applied on the electrodes along the gas cell is presented in Fig. 2b (distribution 1). According to calculations using the SimIon code [15], this distribution should lead to an optimum extraction efficiency, assuming that space-charge effects can be neglected. In the following, this voltage distribution will be referred to as the standard

distribution. The standard voltage distribution divides the gas cell into three regions: (1) the entrance region with a steep, reversed direction of the electrical gradient, (2) the main volume of the gas cell with a moderate almost parallel drifting field, and (3) the region in vicinity of the exit nozzle with a stronger spherical focusing field. Fig. 2b shows also other voltage distributions, that were used in the measurements reported here.

Special effort is required to ensure the purity of the helium gas. Commercially available 99.999% pure helium is further purified by a Nanochem L-2000 filter in a manifold system connected to an oil-free pump. The manufacture's specification for the level of impurities is lower than 1 ppb for H_2O, O_2, CO and CO_2. The gas manifold, the gas cell, and the gas lines are baked under vacuum before each experiment.

The expansion chamber is evacuated by a large industrial booster and mechanical pumping system (2550 l/s). The pressure distribution of the supersonic jet was measured previously by scanning the jet with a Pitot tube [16]. A 2 m long quadrupole radiofrequency quadrupole (rfq) ion-guide (Fig. 1) consisting of four segmented rods [17] serves for guiding the ions that leave the gas cell with the gas jet. The rods are alternatively connected to the opposite poles of an rf voltage supply providing an amplitude up to 300 V peak-to-peak and a frequency of approximately 1 MHz. This creates a trapping potential for the ions. The rfq guide is divided into three sections with a 3 mm diameter skimmer between the first and second sections and a larger diameter aperture between the second and third sections providing differential pumping. The first section is located in the expansion chamber and is evacuated by the large industrial pump. Each downstream section is evacuated by a large (2000 l/s) turbomolecular pump. All electrical connections inside the differentially pumped region are made with Kapton insulated wires. The entire system is made of metal and ceramic materials so that the base pressure in the beam line is on the order of 10^{-8} torr. The typical pressures along the beam line are indicated at the bottom of Fig. 1. The ions undergo collisions with helium atoms as they are transported through the first section of the rfq ion-guide, which provides transverse cooling of the transported beam [18]. In addition, a weak DC potential is applied along the segmented rods of the rfq ion-guide to drift ions towards the collection point.

A thin wire electrode can be introduced into the path of beam in the middle of the third section of the rfq ion-guide (Fig. 1). A potential of -350 V is applied to the wire to ensure collection of the radioactive ions. The wire can be flipped by 90 degrees between collection

and the measuring positions in about 200 ms. Positrons and gamma rays from the collected source on the wire are detected by a 25 mm thick plastic scintillator and by a Ge detector (relative efficiency 120%) placed in close geometry to the source. The plastic detector has a narrow 3 mm wide and 5 mm deep slot in which the wire is introduced. It is difficult to determine the efficiency of the plastic detector due to a lack of calibrated sources with the appropriate geometry. From geometrical considerations the efficiency for detection of positron particles is estimated to be at least 70%. The Ge detector is surrounded by a lead shield to minimize background. The efficiency of the Ge detector was measured with calibrated sources and was founded to be $\approx$0.8% for the 1568 keV gamma ray (the transition from decay of ^{38}Ca).

Each fragment that stops in the helium creates millions of helium ion-electron pairs that also are drifted by the electrical field. A fraction of these electrons is collected and measured on the the first ring electrode in the gas cell (the highest positive potential). The produced positive ions are drifted together with fragments ions towards the nozzle and are jetted into the expansion chamber. A fraction of these ions is also captured by the rf field and is transported to the collection wire. The parameters of the rfq guide are optimized on the collected current. The current collected on the wire is compared with the current measured in a Faraday cup that is placed downstream in the beam line. The comparison shows that almost all of the transported ions are collected on the wire electrode. It is assumed that the efficiency for collection of radioactive ions on the wire is the same as that for collection of the positive ions. The monitoring of positive and negative currents from the gas cell proved to be very useful for understanding the performance of the gas cell (discussed below).

III. EXPERIMENT

A. Range measurements

Mixed ^{38}Ca/^{37}K/^{36}Ar beams at an energy of approximately 92 MeV/u and momentum acceptance of ΔP/P=0.5% or 0.1% were obtained from the A1900 fragment separator by fragmentation of a ^{40}Ca, 140 MeV/u primary beam[14]. The fragments were produced in a 460 mg/cm^2 beryllium target and separated with a 300 mg/cm^2 aluminum achromatic degrader placed in the dispersive plane of the A1900. The rate of beam fragments trans-

ported to the gas cell was varied by introducing attenuators in the primary beam before acceleration. The beam intensity was measured by a thin plastic detector placed in the A1900 dispersive plane or, in the case of higher primary beam intensities, by a BaF_2 detector monitoring the production target reaction rate. The magnetic rigidity, $B\rho$, of the fast ions before the experimental setup was 2.688 T·m. For this particular experiment, the beam energy was degraded by an optically polished 1.501(3) mm thick borosilicate glass plate and an optically polished fused silica wedge that had a median thickness of 0.722(3) mm and a wedging angle of 4.0(5) mrad.

A typical particle identification plot obtained with the Si detector inside the gas cell is shown in Fig. 3a. The full momentum acceptance of 0.5% resulted in the transport of ^{38}Ca ($T_{1/2}$=0.44 s), ^{37}K ($T_{1/2}$=1.22 s) and ^{36}Ar (stable) fragments in the ratio of approximately 5:3:1. The primary beam was attenuated by a large factor (10^3-10^4) in order to keep the implantation rate on the order of a few hundred particles per second during the range measurements. As can be seen in Fig. 3a, the different fragments were well separated in the ΔE-TOF diagram. The counting rate of the ^{38}Ca, ^{37}K and ^{36}Ar fragments was measured as a function of the glass degrader thickness (transmission profile or number-distance curve). The magnetic rigidity of the last two quadrupole elements between the degraders and the gas cell was adjusted for each value of the degrader thickness according to the calculated energy loss in the degrader system. The measurements were performed both for the evacuated gas cell and for 1 bar helium pressure in order to determine the optimum thickness of the glass degrader and the maximum stopping efficiency of the system [8]. The difference between transmission with and without helium as a function of the degrader thickness corresponds to the fraction of the primary ions stopped in gas (stopping profile). The transmission and stopping profiles are presented in Fig. 4a-c for the three fragments.

More tests were performed with the same fragmentation conditions except that a narrower full momentum distribution (ΔP/P=0.1%) was used. The narrower momentum distribution of the projectile fragments was obtained with a 2 mm horizontal slit at an image position (Image-3) of the A1900 separator [14]. The narrow momentum distribution resulted in a ^{38}Ca/^{37}K/^{36}Ar admixture of approximately 25:5:3. The implantation intensity was approximately an order of magnitude lower compared to that for the fragmentation beam with 0.5% momentum spread at the same primary beam intensity. The measurements of the stopping efficiency as a function of degrader thickness were performed as described above. The results

of the stopping range measurements are presented in Fig. 4d-f.

The transmission profiles were first fitted with Fermi functions as in the previous work [8, 12] but these functions do not reproduce very well the present data at the end of the range. Instead the function :

$$f(z) = a \exp(-\exp((z-b)/c))$$

was used to fit the data in Fig. 4, where z is the degrader thickness, a is a normalization constant, which is close to one for ^{38}Ca, b is the midpoint and c is the width parameter of the declining part of the function.

The agreement of the range measurements for the two momentum distributions is excellent at the level of a few microns of the degrader thickness, given that the experiments were separated by a few weeks in time requiring a complete retuning of the NSCL facility. The range distributions for the two values of the beam momentum spread have a similar width which is due to the straggling in the 1022 μm beryllium window. The typical variation of the Be window thickness is 1.5-2 microns that corresponds to 1.5-2 10^{-3} relative thickness variation. According to the ref. [11] thickness tolerances needed to be on the level of a few 10^{-4}. It is difficult to acheive such tolerance for a 1 mm thick degrader. The width of the ^{38}Ca stopping profile obtained for the ΔP/P=0.1% momentum spread is on the order of 31 μm of glass, while calculations performed with the LISE++[20] or MOCADI[21] codes predict much narrower widths for the range distribution ($\approx$18 μm of glass). The ATIMA stopping power model [22] was used in the both codes. The fitted stopping profiles exhibit a skewness towards low degrader thickness values, unlike the results of similar earlier measurements [8, 12]. The data from the earlier experiments were obtained using a pair of glass degraders that were rotated in opposite directions to compensate, to first order, for the small horizontal angular divergence of the beam. The use of a single degrader plate in the present experiment may have resulted in a different shape of the stopping profiles and effectively broader range distribution. Furthermore a Si telescope assembly was used in [8, 12] allowing identification of secondary reaction products (a few per cent of total beam intensity) arising from passage of the fragments through the degraders and the beryllium window. Such identification was not possible in the present experiment, resulting in an additional uncertainty in the measurements at the end of the range.

B. Collection of induced ionization charge

One of the inherent problems for the collection of fast ions is the fact that the stopping of each incident ion creates millions of ion-electron pairs in the buffer gas. This is illustrated in Fig. 5a where the rate of energy loss in helium (1 bar) was calculated with the SRIM2003 code [23] for a ^{38}Ca beam that passed through the glass degrader with an effective thickness of 1715 μm, the wedge (722 μm), and the beryllium window (1022 μm). This configuration corresponds to that for which the maximum extracted yield was obtained, as will be discussed below. The calculated longitudinal distribution of the thermalized ^{38}Ca ions is shown in Fig. 5b. One can see that the fast ions come to rest beyond the peak of the ionization for the narrowest momentum distributions. However, even for modest momentum distributions, this separation will practically dissappear. The situation is even more complicated with mixed beams of projectile fragments. In the present work, the ^{37}K ions stop in the wakes of the ^{38}Ca ions.

The production and collection of ions and electrons from buffer gas ionization was studied in a measurement using a ^{48}Ca primary beam. The final beam energy before entering the beryllium window of the gas cell was rather high, $\approx$ 47 MeV/u. At this energy, the primary ions passed through the gas cell and struck the nozzle. This produces an approximately uniform ionization rate along the path and simplifies the interpretation of the results of the measurements. Use of a primary, rather than a secondary beam, also allowed for a broader range of implantation rates during this measurement. The positive ion current was collected on a foil placed directly in the jet in the geometry described in [13] (the collection of the ions in the jet was more efficient than the collection on the wire electrode after the two meter long rfq guide). The standard voltage distribution along the gas cell was scaled down by a factor 0.5 to avoid sparking in the gas cell at the highest implantation rates. A -300 V bias was applied to the collection foil. A fraction of the electron current was collected on the first ring electrode. In Fig. 6a the negative and positive currents are shown as a function of implantation rate and compared with the calculated induced ionization. The data show that the collected negative current is proportional to the calculated induced ionization, but is lower by a factor of $\approx$25. This factor is due to the rather low electron collection efficiency on the first ring which was confirmed by SimIon calculations. Most of the collected electrons come from the first region of the gas cell between the entrance window and the first ring,

the remainder of ionized electrons is collected on other ring electrodes.

The positive current measured on the foil outside the gas cell is found to only increase with the square root of the primary ionization. Recall that the positive ions are collected after drifting a large distance before being focused and extracted through the nozzle. It is likely that the positive ion density produces a space-charge buildup that pushes ions in the transverse direction. Depending on the charge density, a large fraction of the helium ions may never reach the area where the gas flow takes over the ion transport.

The difference between the behavior of the negative and positive ion currents is more apparent in Fig. 6b where the ratios of the measured current to that expected on the basis of the calculated ionization of the helium buffer gas are shown. The ratio for negative current is a constant factor at low implantation rates. Above a rate of approximately 10^6 pps the observed ratio drops in proportion to $R^{-1/4}$. The constant reduction at low rates can be attributed to the poor collection efficiency of electrons on the first ring previously mentioned above. The decrease above 10^6 pps rate can be understood as the result of the induced field due to the space-charge. On the other hand, the ratio of the observed positive ion current to the induced ionization steadily decreases in proportion to $R^{-1/2}$ over the full range of measured implantation rates.

C. Extraction of fragments

The efficiency for extraction of the fragment beams was obtained from the radioactive decay of the ions that, after stopping in the gas cell, were transported by the drifting fields towards the nozzle, extracted by the jet to the low pressure region, captured and transported by the rfq guide and collected on the thin wire. As expected, the counting rate in the plastic detector from the activity collected with a positive voltage on the wire (repulsion of positive ions) was much lower than that observed with a negative voltage on the wire (collection of positive ions). An example of a decay curve measured in the plastic detector and a typical positron-gated gamma-spectrum are shown in Fig. 7a and 7b, respectively.

The extraction efficiency can be obtained from the ratio of the counting rate in the beta detector to the deduced ^{38}Ca and ^{37}K implantation rate corrected for positron detection and time cycle efficiencies. The fragment implantation rates were estimated using the counting rate in the BaF_2 target monitor. This monitor was calibrated at the lower implantation rates

using the Si detector inside the gas cell. It was assumed that fragment implantation intensity scaled with the BaF_2 counting rate up to the highest primary beam intensity. The extraction efficiencies measured at different implantation rates as a function of degrader thickness are compared to the combined stopping profile as shown in Fig. 8a. The experimental stopping curves for ^{38}Ca and ^{38}K measured with the silicon surface barrier detector at a distance of 39 cm from the beryllium window, shown individually in Fig. 4, were combined and corrected for the additional 12 cm of helium (7μm of glass equivalent). The main systematic errors in the measurements of extraction efficiency are associated with the determination of the implantation rate with the BaF_2 detector and the uncertainty of the efficiency of positron detection. The peak extraction efficiency is approximately 5% and occurs at a degrader thickness of 1715 μm at low implantation rates.

It is evident from Fig. 8a that : (1) The extraction efficiency decreases at the implantation rates higher than 500 pps and (2) the extraction efficiency is shifted slightly with respect to the stopping efficiency curve towards higher values of the degrader thickness. The reduction of the extraction efficiency with the implantation rate is probably due to the induced ionization of helium.

The variation of the positive and negative currents as a function of degrader thickness is shown Fig. 8b. The data were obtained at the relatively high implantation rate of ~40k pps. Both currents depend on the total ionization created in the gas volume (see for example Fig. 5a). However, the negative current also reflects the fact that the electron collection on the first ring inside the gas cell is more efficient for the charges created in the first region of the cell. The negative current peaks near the maximum of the extracted yield and the maximum of the range distribution (cf. Fig.8a) when a considerable ionization is produced in the region close to the first ring (Fig. 5a). On the other hand, the positive current is measured after the exit nozzle. The positive ion current is a factor of five lower overall than the negative current even though the collection efficiency for the negative current is very low (0.04 was observed for uniform ionization discussed above). Moreover, the positive current is suppressed in the region of the optimum extraction. The suppression of the positive current takes place for an ionization distribution that has a large part of ions created in the upstream half of the cell (Fig. 5a). The produced ions have to travel a longer distance, on average, through the cell than the fragment ions (Fig. 5b). A longer distance and longer drift time makes the ions sensitive to losses. The majority of ions created in the first part

of the cell will be collected on the beryllium window due to the reversed electrical field in the first region of the cell, which also contributes to the current suppression at the largest degrader values.

The influence of the transport efficiency of the helium ions to the nozzle region was tested by scaling the magnitude of the drift field while maintaining the overall shape of the potential. The relative efficiency for fragment collection obtained from the observed beta-decay rate is shown as a function of the voltage scaling factor in Fig. 9. The glass degrader was set to the peak extraction efficiency ($1715\mu m$) and the fragment implantation rate was approximately 5k pps. The relative efficiency decreases linearly by a factor of approximately four when increasing the scaling factor from 0.15 to 1.7. Given the constant degrader thickness and constant implantation rate, the largest effect of changing the voltage is to increase the longitudinal drift velocity of the positive ions. For example, the maximum drift times calculated with SimIon (without space-charge effects) for the lowest and highest field strengh are 510 and 65 ms, respectively. These drift times should be compared to a value of 100 ms obtained for the standard voltage distribution. With higher longitudinal velocities, we expect that space charge is reduced in the main volume of the cell and that the positive ions suffer smaller losses during their transport to the nozzle. The drop in the number of extracted radioactive ions can then be understood as due to an increased space-charge effect from the positive charge in the nozzle region.

In order to study the effect of the guiding field in the gas cell further, another series of measurements was performed using the $^{38}Ca/^{37}K$ beam with a 0.1% momentum distribution. As shown in Fig 5, these fragments and the bulk of the helium buffer gas ions should have some longitudinal separation. The extraction efficiency was measured as a function of degrader thickness for the four voltage distributions shown in Fig. 2b. The four distributions were chosen such that the electric field in the spherical region near the nozzle remaines constant (region three in Fig. 2) with a maximum potential upstream in the cell. The first distribution is the standard distribution used in all the measurements discussed up to this point. Except for a fraction of ions close to the beryllium window, all ions will be guided towards the nozzle. The position of the highest voltage was moved toward the nozzle for the other voltage distributions. The fourth distribution is expected to only collect ions that come to rest in the region of the spherical electrodes near the nozzle. All other ions will be guided away from the exit hole of the gas cell. The results for the extraction efficiency

as a function of degrader thickness and voltage distribution are shown in Fig. 8c. The peak extraction efficiency with the standard voltage and a narrow momentum distribution appears to be insignificantly larger than that found for the broader momentum distribution under similar experimental conditions (triangles in Fig. 8a). It is interesting to see that the efficiencies obtained with distributions #1 and #2 are very similar even though the volume from which ions are guided to the extraction is quite different. The width of the extraction efficiency curve decreases when the position of maximum voltage moves closer to the nozzle as it is in the case of distributions #3 and #4. The maximum efficiency drops and the peak position moves to lower degrader thicknesses. This is consistent with collection of the ions from the volume of the gas cell close to the exit nozzle.

The measured extraction efficiency and the extracted yield are displayed as a function of implantation rate in Fig. 10. All of the measurements were taken with the standard voltage distribution (#1) and the optimum degrader thickness ($\sim 1715\mu m$) for both momentum distributions. The maximum extraction efficiency is seen at the lowest implantation rates and there is some indication that the efficiency levels off near 2000 pps.

IV. DISCUSSION

The conversion of a energetic projectile fragment beam into a beam of thermalized ions was demonstrated in the present work. An extraction efficiency from a high-pressure drift gas-cell on the order of a few percent was achieved for $^{38}Ca/^{37}K$ fragmentation beams under a number of different conditions. The extraction efficiency was studied as a function of degrader thickness for a number of longitudinal drift voltage conditions and various implantation rates. The results of the measurements suggest that there are several loss mechanisms associated with the ionization of the buffer gas created by the electronic stopping of the radioactive ions.

In the absence of electric fields, as in IGISOL systems, the neutral plasma is carried by the gas flow towards the exit nozzle. The high density of ion-electron pairs results in some neutralization of the stopped reaction products and ionized buffer gas via 3-body recombination between the singly charged ions, electrons and neutral helium. In the NSCL gas cell a longitudal electric field is applied to separate the ion-pairs and to drift the cations to the exit nozzle. Thus, the gas cell works in the regime similar to that of ionization chambers.

The first loss mechanism is associated with screening of the applied electrical field by the field induced by the space-charge of the created ions. This subject was addressed in detail recently by Huyse et al. [24]. They analyzed the space-charge effects in the framework of an idealized infinite parallel plate drift chamber filled with a uniform rate of ionization. Eq. 9 from [24] can be used to establish the variation of the induced voltage, $V_{induced}$, over the plate separation, d, as:

$$V_{induced}/d = \sqrt{eqRd/4\epsilon_0\mu_+ A}$$

where e is the charge on the electron, q is the primary charge in Coulombs created by one implanted ion, R is the implantation rate per second, ϵ_0 is the permittivity of vacuum, μ_+ is the mobility of the buffer gas ions, and A is the area of the column of charge. The conditions of the experiment with the ^{48}Ca primary beam (section IIIB) correspond to a uniformly ionized cylindrical chamber (radius= 1.4 cm). The resulting values for the ionization density, $Q = qR/dA$, and the voltage induced by the space-charge are given in Table I as a function of implantation rate, R of the ^{48}Ca primary beam. As the negative current measured on the first ring was collected mostly from the first region of the gas cell a value of d in the equation above is taken to be 6.5 cm. According to the calculations in the table recombination losses are negligible in this system up to very high implantation rates. The calculations also indicate that the applied voltage of 650 V should be screened by the induced field at an implantation rate of approximately 10^6 ions/s for this idealized drift chamber. The critical implantation rate at which the collected negative current begins to deviate from the linear dependence (Fig. 6) is in agreement with the prediction of Table I. The reduction of the applied longitudinal drift field by the space-charge induced field will lead to longer drift times allowing radioactive decay losses and, for highest rates, neutralization losses resulting in lower extraction efficiencies. The potential gradient in the second part of the gas cell is significantly lower so it can be expected to be affected even at lower implantation rates.

Raising the applied electric field to a value sufficient to overcome the effect of the induced field is not practical because the low dielectric strength of helium gas puts a limit on the drift voltage that can be applied inside the gas cell. For reference, the breakdown voltage at normal pressure in helium is approximately six times lower than that in air [25]. Application of 5 kV to the d=50 cm long cell at 1 bar is somewhat difficult and would only result in an electrical field of $E_{applied}$=100 V/cm. An option to minimize space charge effects is to increase

the area over which the ions are implanted. Given that the area over which ionization is created is about of 6 cm^2 in the present work, a gain of more than two orders of magnitude larger area is not possible.

The second mechanism responsible for the loss of implanted fragments and the helium ions in the region far from the nozzle is migration along a radial space-charge potential. The space-charge induces a radial field gradient that will push ions out of the ionization volume during their longitudinal drift. The first results from a self-consistent calculation of ion migration in the cylindrical region of the gas cell including space-charge effects indicate that the radial potential is on the order of 25 V in the present case at implantation rates above 10^4 pps. These first results appear to be in good agreement with the present work and a detailed publication is being prepared [26].

The third factor responsible for the loss of the implanted fragments is associated with the passage of all of the positive ions through a small (0.8 mm diameter) nozzle. An estimate shows that the charge density in the vicinity of thr nozzle is two orders of magnitude higher than the typical density in the drifting region of the gas cell. This estimate is based on the ion velocity in the electrical fields calculated for the standard voltage distribution using the SimIon code. The ion velocity is determined by the gas flow only a few millimeters from the nozzle according to the VARJET code [27]. The space-charge effects in such a small column will be larger than those in the drift region leading to significant loss in the extraction. As is seen in Fig 6, the ratio of the extracted ionic current to the calculated ionization drops with the square-root of the implantation rate. This drop is due to the lateral escape of ions during their drift and in the nozzle region (the second and third ion loss mechanisms). Extrapolating the square-root dependence of the extracted positive ion current in Fig. 6b to the low implantation rates, we find that the observed current would be equal to the expected one at a rate of $\approx$50 ion/s (if the collection efficiency on the foil in this test was near unity). Therefore, we expect that the space-charge effects associated with the passage through the nozzle region are important even at such low implantation rates. These are rates at which the lateral escape due to the radial drift is not so important.

The extraction efficiency for fragments also decreases roughly with the square-root of the implantation rate (Fig. 10). The extracted yield correspondingly increases in proportion to the square root of the implantation rate in a similar manner to the increasing positive ion current observed in the test with ^{48}Ca primary beam. The square-root dependence observed

here is similar to that observed by Wada et al. [6] for high energy $^{8}Li^{+}$ ions extracted from a transverse drift gas cell using a weak collection field and an rf-carpet near the nozzle. Kudryavtsev et al. [28] also showed that the extraction of thermalized $^{58}Ni^{+}$ ions from the small LISOL gas cell without a drift field and without laser re-ionization follows a power law (cf. Fig. 4b in [28]) albeit at a very low efficiency. In all these experiments ions were collected after the passage through a narrow exit hole. Thus, the square-root dependence on the implantation rate associated with the space-charge effects in a gas cell may be a common attribute of gas cell devices.

The three interconnected ion-loss mechanisms associated with ionization in helium are reduction of drifting electrical fields by space-charge buildup, lateral escape of the drifting ions due to the radial potential associated with space-charge buildup, and space-charge effects in the region of the exit nozzle. These ion-loss mechanisms provide a qualitative explanation of the results of the tests presented in Figs. 6,8,9,10. Both the stopped fragment ions and the created helium ions experience loss during extraction. However, the losses are higher for helium ions than for the fragments, due to their longer drift distances, on average, in the cell. Thus, some low-level segregation between the fragments and helium ions takes place in the present gas cell allowing one to achieve moderate extraction values. Alternative electrode designs with more focusing or segregating the projectile fragments from the bulk of the ionization may be possible. The helium ions have to be separated from the heavier projectile fragments in the gas before they reach the nozzle region. RF-funnel devices that operate at lower pressures can provide such separation of helium buffer gas from significantly heavier implanted ions [5, 6]. The development of a funnel that can be operated under the high-pressure conditions in the NSCL gas cell is underway.

The chemical composition of the extracted radioactive ions was not investigated in the present work. Chemical processes taking place in the NSCL gas cell together with the influence of the gas purity will be addressed in future work.

V. CONCLUSION

The initial tests of ion stopping and collection from the NSCL have demonstrated the feasibility of the conversion of energetic, 92 MeV/u, $^{38}Ca/^{37}K$ fragmentation beams into beams of thermalized ions. The extraction efficiency of the order of a few per cent was obtained.

This efficiency is sufficient to begin a broad experimental program with thermalized, rare-ion beams at the NSCL. There is growing evidence that the space charge due to the primary unavoidable ionization seriously limits the efficiency of gas cell systems. Further studies of the ion collection, as well as, further improvements of the gas cell system are underway.

We are grateful to Jack Ottarson for his help in designing all of the components of the NSCL gas cell and to the staff of the NSCL cyclotron facility and especially the A1900 separator crew for providing reliable beams during the course of this work. This work was supported by the National Science Foundation grant PHY-01-10523 and by the US Department of Energy grant 00ER41144.

---

[1] B.M. Sherrill, Nucl. Instr. and Meth. **B204** (2003) 765.

[2] G. Savard, Nucl. Instr. and Meth. **B204** (2003) 771.

[3] J. Vervier, Nucl. Instr. and Meth. **B204** (2003) 759.

[4] G. Sikler *et al.*, Nucl. Instr. and Meth. **B204** (2003) 482.

[5] G. Savard *et al.*, Nucl. Instr. and Meth. **B204** (2003) 582.

[6] M. Wada *et al.*, Nucl. Instr. and Meth. **B204** (2003) 570.

[7] S. Schwarz *et al.*, Nucl. Instr. and Meth. **B204** (2003) 507.

[8] L. Weissman, D. Davies, P.A. Lofy and D.J. Morrissey, Nucl. Instr. and Meth. **A522** (2004) 212.

[9] H. Geissel, Th. Schwab, P. Armbruster, J.P. Dufour, E. Hanelt, K.-H. Schmidt, B. Sherill, G. Münzenberg, Nucl. Instr. and Meth. **A282** (1989) 247.

[10] H. Weick *et al.*, Nucl. Instr. and Meth. **B164-165** (2000) 168.

[11] C. Scheidenberger *et al.*, Nucl. Instr. and Meth. **B204** (2003) 119.

[12] L. Weissman, D. Davies, P.A. Lofy and D.J. Morrissey, Nucl. Instr. and Meth. **A531** (2004) 416.

[13] L. Weissman, P.A. Lofy, D.A. Davies, D.J. Morrissey, P. Schury, S. Schwarz, T. Sun and G. Bollen, Proc. RNB6, G. Savard, Ed., Nucl. Phys. **B** (2004) in press.

[14] D.J. Morrissey, B.M. Sherrill, M. Steiner, A. Stolz and I. Wiedenhoever, Nucl. Instr. and Meth. **B204** (2003) 90.

[15] computer code SimIon, available from `http://www.sisweb.com/simion.htm`

[16] P.A. Lofy, Ph.D. Dissertation, Michigan State University, 2003.

[17] F. Herfurth *et al.*, Nucl. Instr. and Meth. **A469** (2001) 254.

[18] H.J. Xu, M. Wada, J. Tanaka, H. Kawakami, I. Katayama and S. Ohtani, Nucl. Instr. and Meth. **A333** (1993) 274.

[23] J. F. Ziegler, computer code SRIM-2003, available from `http://www.srim.org/SRIM`.

[20] D. Bazin, O. Tarasov, M. Lewitowicz, O. Sorlin, Nucl. Instr. and Meth. **A 482** (2002) 314, available from `http://groups.nscl.msu.edu/lise/lise.htm`

[21] http://www-linux.gsi.de/~weick/mocadi/

[22] C. Scheidenberger and H. Geissel, Nucl. Instr. and Meth. **B135** 25 (1998) and http://www-aix.gsi.de/~scheid/ATIMA1.html

[23] J. F. Ziegler, computer code SRIM-2003, available from `http://www.srim.org/SRIM`.

[24] M. Huyse, M. Facina, Yu. Kudryavtsev and P. Van Duppen, Nucl. Instr. and Meth. **B187** (2002) 535.

[25] K.H. Mess, P. Schmüser, S. Wolff, "Superconducting accelerator magnets", (World Scientific Publishing Co. Pte. Ltd., Singapore, 1996) pp. 201-202.

[26] S. Schwarz *et al.*, to be published.

[27] V.L. Varentsov and A.A. Ignatiev, Nucl. Instr. and Meth. **A413** (1998), 447.

[28] Yu. Kudryavtsev, M. Facina, M. Huyse, J. Gentens, P. Van den Bergh, P. Van Duppen, Nucl. Instr. Meth. **B204**(2003) 336.

TABLE I: Calculated ionization rate, recombination fraction, and induced voltage for conditions similar to that in in the first region of the gas cell are given as a function of the incident ^{48}Ca projectile rate. The expressions in [24] were used for a parallel plate drift chamber having a distance between the plates of 6.5 cm. The induced ionization was assumed to be contained in a cylinder with a radius 1.4 cm. The induced voltage should be compared to 650 V applied voltage.

Incident Rate, R (/s)	Ionization density, Q, (ion-electron pairs/cm^3/s)	Recombination losses	$V_{induced}$ (volts)
10	$5{\cdot}10^{4}$	$5{\cdot}10^{-10}$	2.0
10^2	$5{\cdot}10^{5}$	$5{\cdot}10^{-9}$	6.2
10^3	$5{\cdot}10^{6}$	$5{\cdot}10^{-8}$	$2.0{\cdot}10^{1}$
10^4	$5{\cdot}10^{7}$	$5{\cdot}10^{-7}$	$6.2{\cdot}10^{1}$
10^5	$5{\cdot}10^{8}$	$5{\cdot}10^{-6}$	$2.0{\cdot}10^{2}$
10^6	$5{\cdot}10^{9}$	$5{\cdot}10^{-5}$	$6.2{\cdot}10^{2}$
10^7	$5{\cdot}10^{10}$	$5{\cdot}10^{-4}$	$2.0{\cdot}10^{3}$
10^8	$5{\cdot}10^{11}$	$5{\cdot}10^{-3}$	$6.2{\cdot}10^{3}$
10^9	$5{\cdot}10^{12}$	$5{\cdot}10^{-2}$	$2.0{\cdot}10^{3}$

FIG. 1: Schematic diagram of the experimental equipment. The indicated distances are not to scale. Two quadrupole magnets placed between the degraders and the gas cell are not shown. The pressure values along the beam line are indicated.

FIG. 2: (a) Schematic diagram of the gas cell. (b) Different voltage distributions on the gas cell electrodes used in the measurements. Three regions of the gas cell created by the standard voltage distribution (distribution 1) are indicated.

FIG. 3: Typical ΔE-TOF plots used for particle identification. (a) Spectra obtained with a nominal momentum distribution of 0.5%, without gas and with a 1.5 mm thickness of the borosilicate glass degrader. (b) Similar to (a) for a narrow momentum acceptance of 0.1%

FIG. 4: The rate of the ^{38}Ca, ^{37}K and ^{36}Ar fragments as a function of degrader thickness measured for evacuated chamber and for 1 bar pressure, The transmission (solid lines) and stopping profiles (dahed lines) obtained for each fragment are presented. The data in (a-c) were obtained for $\Delta P/P$=0.5% and in (d-f) for $\Delta P/P$=0.1% beam momentum distributions.

FIG. 5: (a) The calculated rate of ionization along the path of ^{38}Ca ions in 1 bar helium after passing through a 1715 micron glass degrader, the glass wedge degrader, and the beryllium window. This glass degrader thickness corresponds to that for which a maximum extraction yield was achieved in the measurements. The curves correspond to different momentum spreads, $\Delta P/P$, of the beam as indicated. (b) The normalized probability distributions of the final position of ^{38}Ca ions corresponding to the curves shown in (a) calculated with the SRIM2003 code [23]. The bin size is 25 mm. The variations in the degraders thicknesses are not taken in account in this calculation. The curve that sharply peaks at 100 mm is the calculated drift time for positive ions in the cell for the standard voltage distribution shown in Fig. 2b.

FIG. 6: (a) The positive and negative currents (squares and triangles, respectively) as a function of the implantation rate R of ^{48}Ca beam are compared with the calculated ionization (solid line). The corresponding ionization rate is also indicated. The ^{48}Ca beam had an energy of approximately 47 MeV/u before entering in the gas cell window. Scaled R, $R^{1/2}$ and $R^{3/4}$ dependencies (thin lines) are overlaid on the data. The implantation rate where the negative current measurements start to deviate from the linear dependence is indicated by an arrow. (b) Ratios of the positive and negative collected currents to the calculated ionization rate (squares and triangles, respectively). Scaled constant, $R^{-1/2}$ and $R^{-1/4}$ dependencies (thin lines) are overlaid on the data.

FIG. 7: (a) A typical time profile of the activity collected for three seconds measuring period is shown. (b) A typical beta-gated gamma ray spectrum observed during these measurements. The positron anihilation peak and 1568 kev peak belonging to ^{38}Ca decay can be observed.

FIG. 8: (a) A summary of the measured extraction efficiency as a function of degrader thickness and implantation rate for fragments with a momentum spread of 0.5% and the standard drift voltages. The measurements were performed for implantation rates of 19500, 6050, 2150, 450 and 75 pps (open circles, squares, triangles, rhombs and full circles respectively). The stopping profile of ^{38}Ca and ^{37}K ions from Fig. 3a scaled by a factor of 0.2 is shown for better comparison. (b) The measured positive and negative currents are shown as a function of degrader thickness obtained under the same conditions as (a) and at a rate of $\approx$50k pps. (c) Measured extraction efficiency as a function of degrader thickness and drift voltage distribution for fragments with a momentum spread of 0.1% and an implantation rate of $\approx$2k pps. The numbers refer to the potential distribution in Fig. 2b.

FIG. 9: Relative extraction efficiency obtained for the optimum degrader thickness (1715 μm) and for implantation rate of $\sim$ 2k pps as a function of the applied drift field voltage strength.

FIG. 10: Measured extraction efficiency (a) and extracted yield (b) as a function of the implantation rate at the optimum degrader thickness and with the standard drift field voltage distribution. Different symbols denote the results from three different experiments with ΔP/P=0.1% (open circles) and 0.5% (rhombs, triangles and squares).

Figure 1

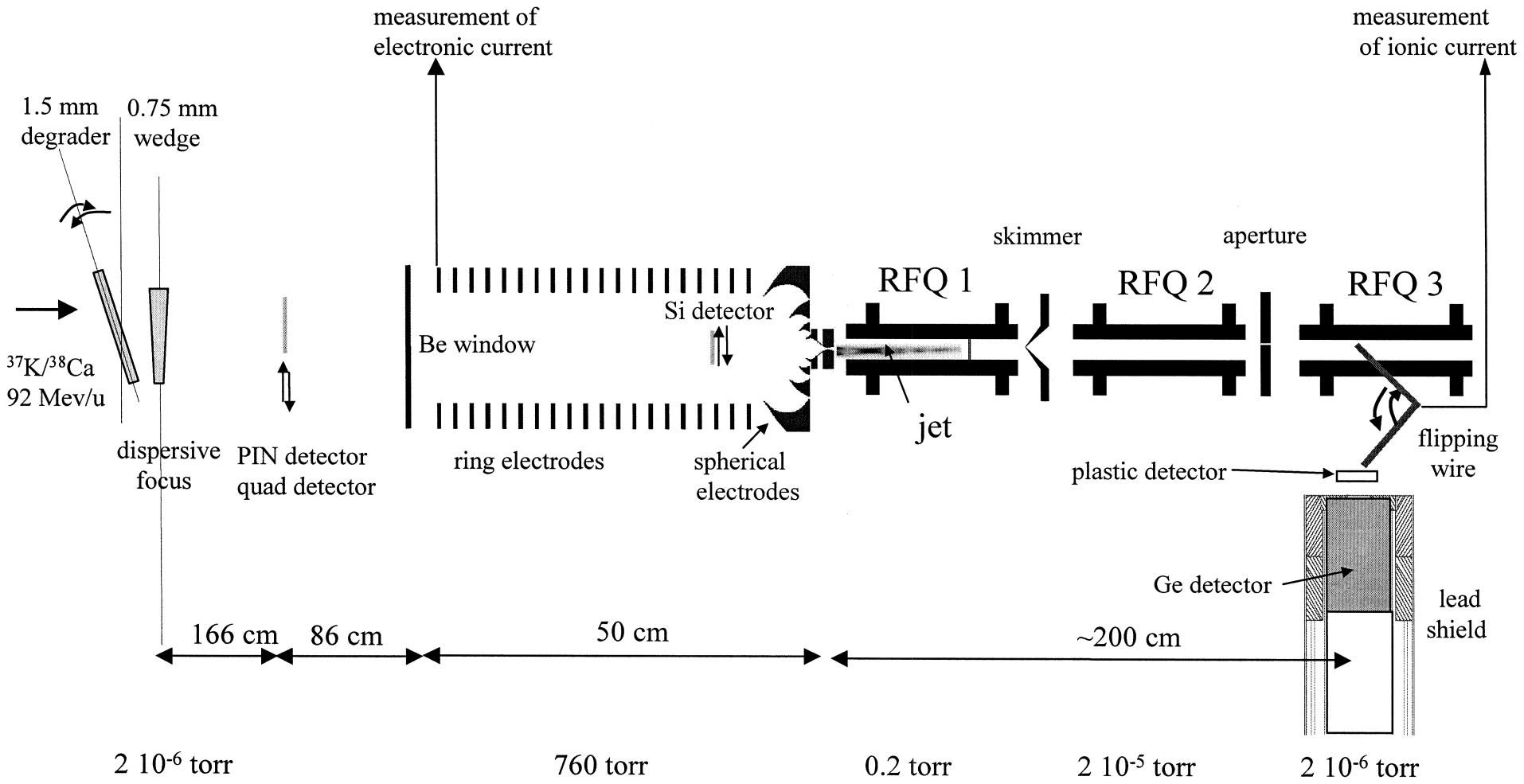
measurement of
electronic current
measurement
of ionic current
1.5 mm
degrader
0.75 mm
wedge
skimmer
aperture
RFQ 1
RFQ 2
RFQ 3
Si detector
Be window
^{37}K/^{38}Ca
92 Mev/u
jet
dispersive
focus
PIN detector
quad detector
ring electrodes
spherical
electrodes
plastic detector
flipping
wire
Ge detector
lead
shield
166 cm
86 cm
50 cm
~200 cm
2 10^{-6} torr
760 torr
0.2 torr
2 10^{-5} torr
2 10^{-6} torr

Figure 2

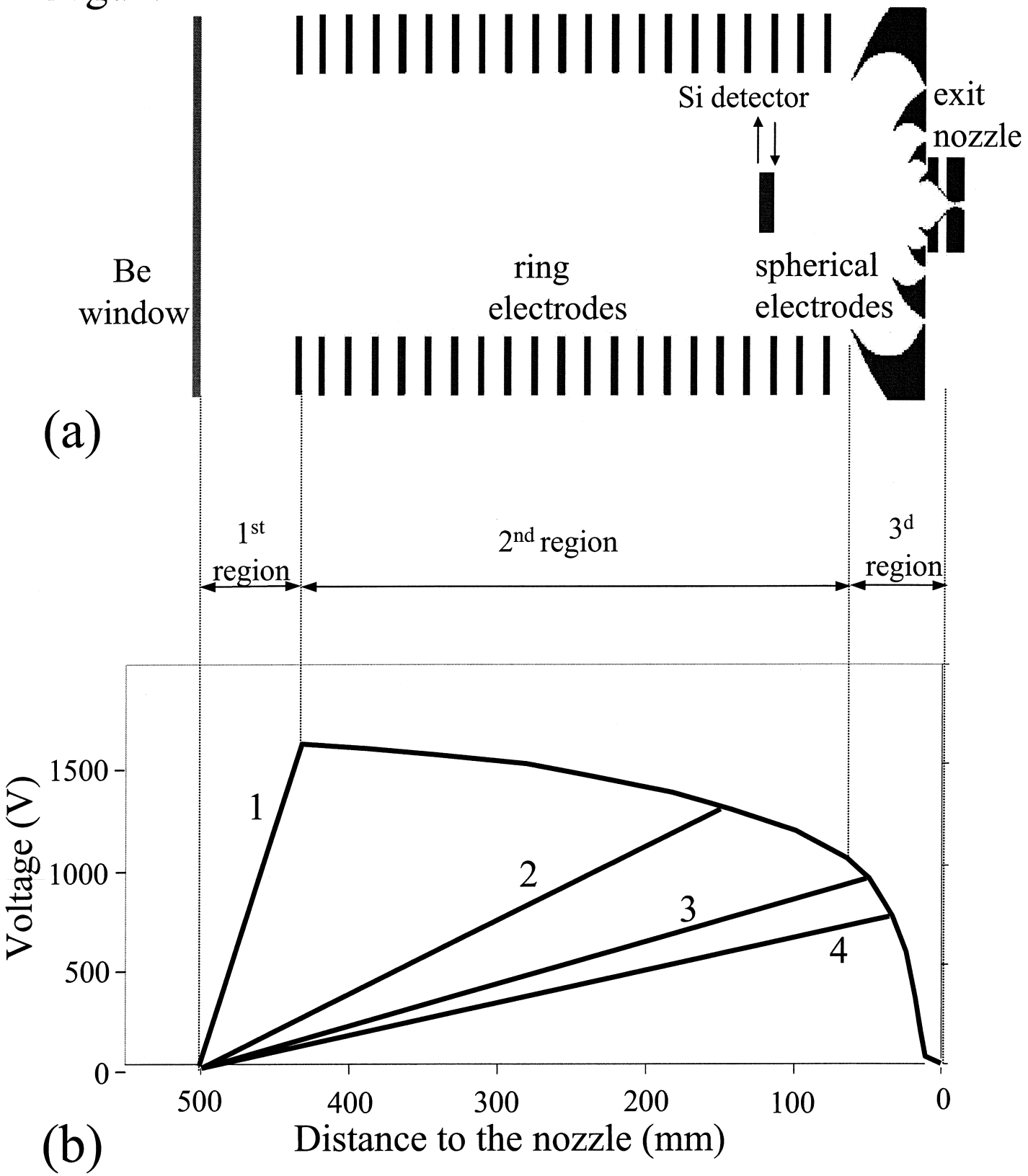
Si detector
exit
nozzle
Be
window
ring
electrodes
spherical
electrodes
(a)
1st
region
2nd region
3d
region
1500
1000
500
0
Voltage (V)
1
2
3
4
500
400
300
200
100
0
Distance to the nozzle (mm)
(b)

Figure 3

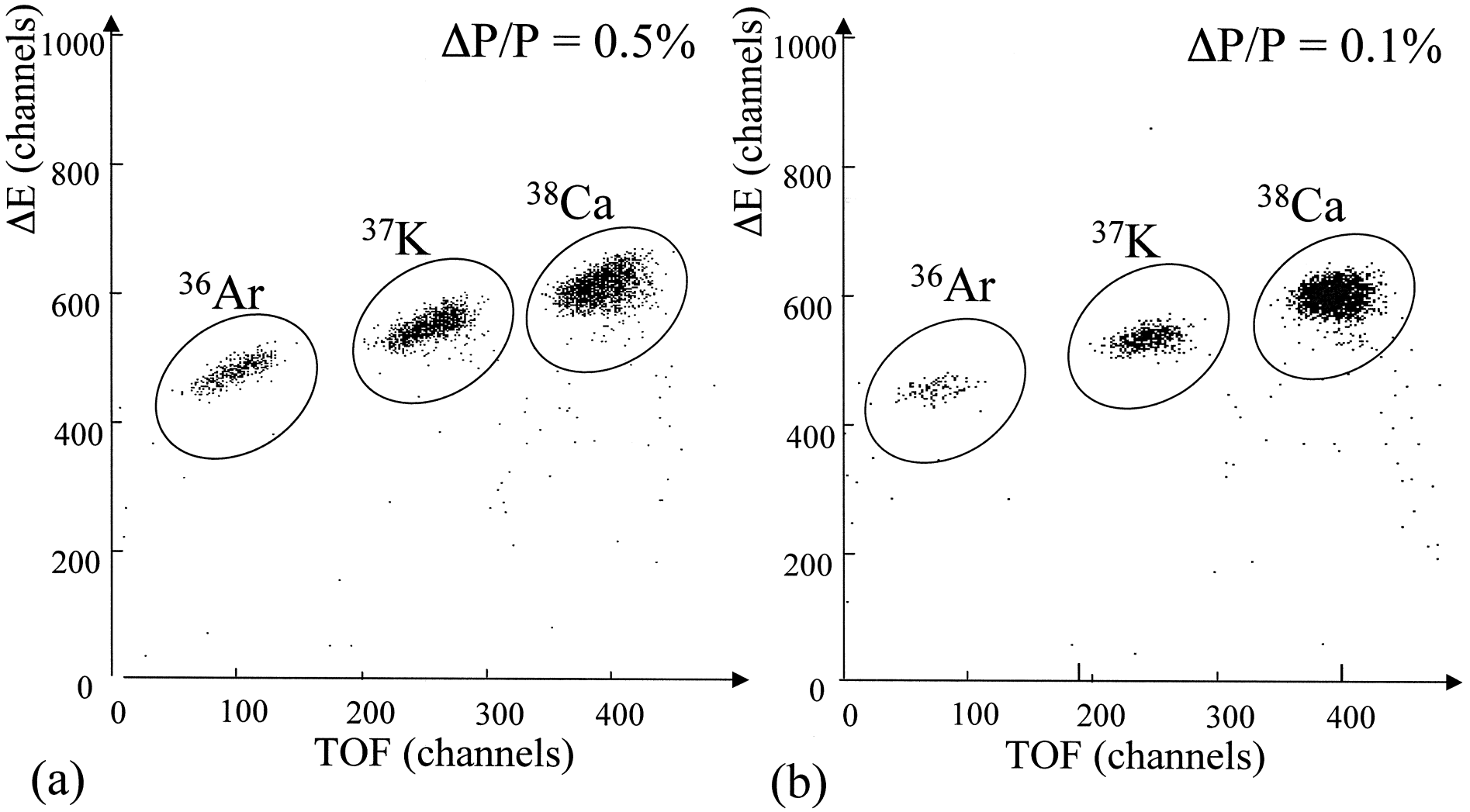
ΔP/P = 0.5%
ΔE (channels)
1000
800
600
400
200
0
0
100
200
300
400
TOF (channels)
36Ar
37K
38Ca
(a)
ΔP/P = 0.1%
ΔE (channels)
1000
800
600
400
200
0
0
100
200
300
400
TOF (channels)
36Ar
37K
38Ca
(b)

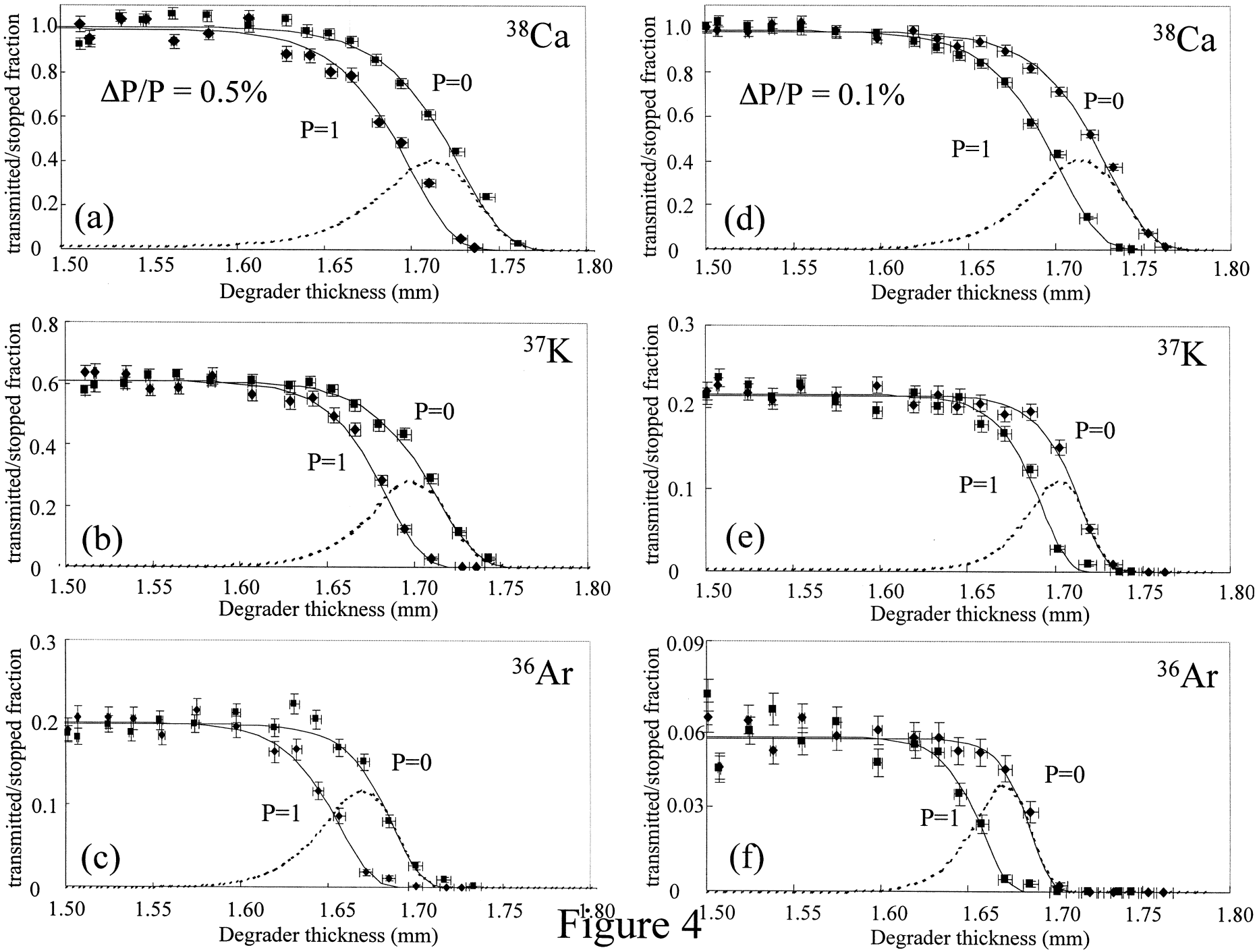
(a)
^{38}Ca
ΔP/P = 0.5%
P=0
P=1
(b)
^{37}K
P=0
P=1
(c)
^{36}Ar
P=0
P=1
(d)
^{38}Ca
ΔP/P = 0.1%
P=0
P=1
(e)
^{37}K
P=0
P=1
(f)
^{36}Ar
P=0
P=1
transmitted/stopped fraction
Degrader thickness (mm)

Figure 4

Figure 5

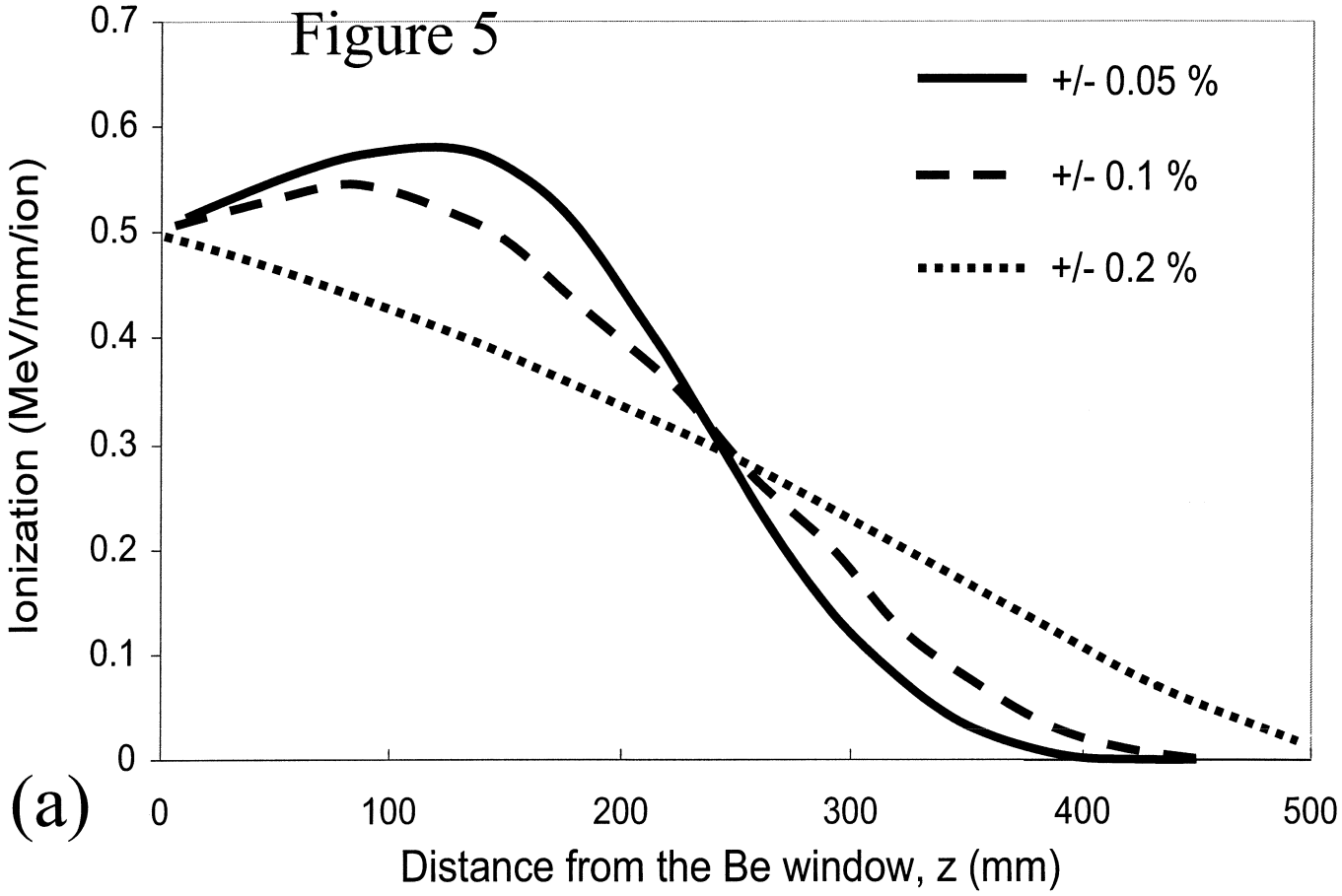
0.7
0.6
0.5
0.4
0.3
0.2
0.1
0
Ionization (MeV/mm/ion)
+/- 0.05 %
+/- 0.1 %
+/- 0.2 %
0
100
200
300
400
500
Distance from the Be window, z (mm)

(a)

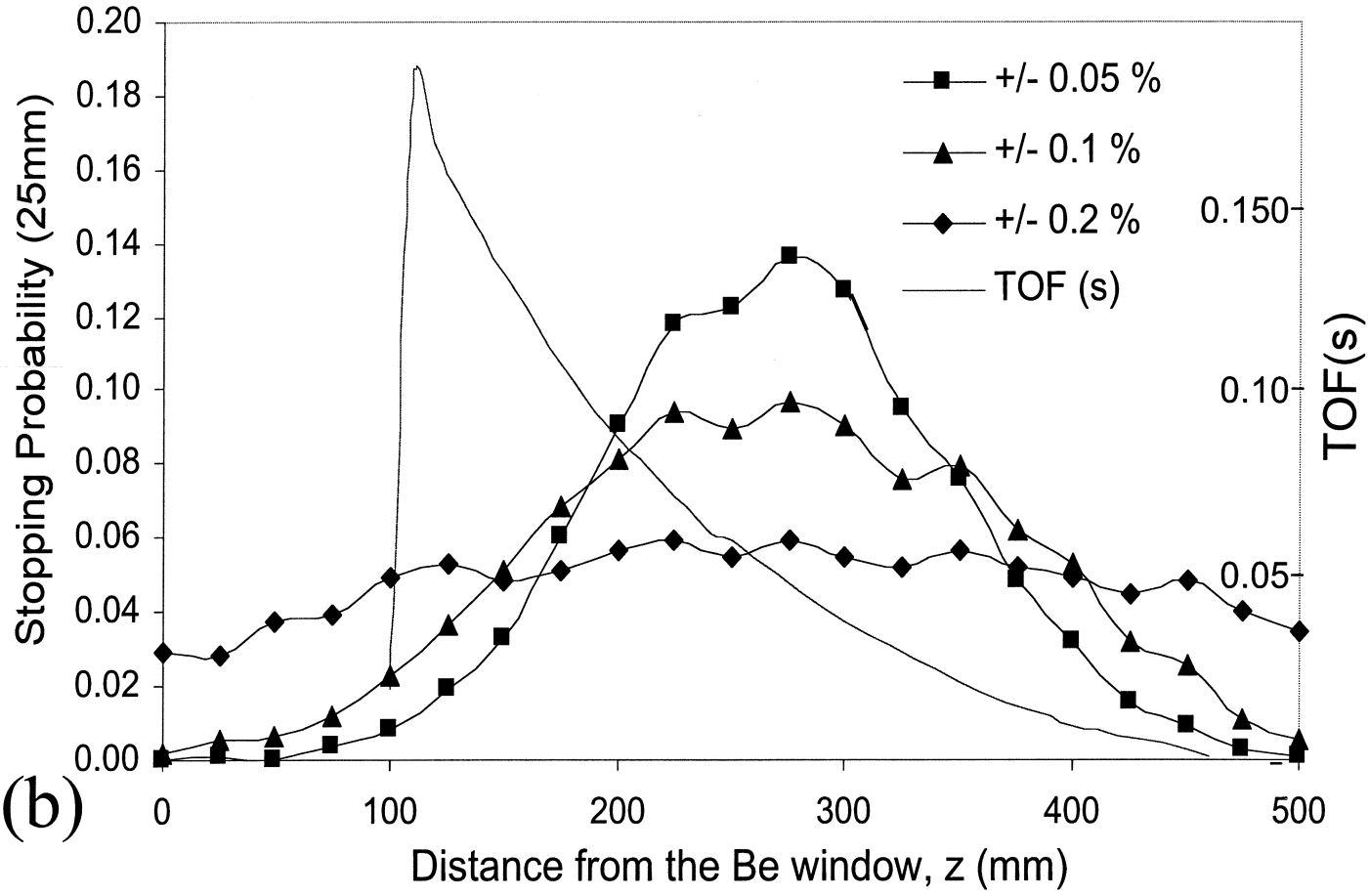
0.20
0.18
0.16
0.14
0.12
0.10
0.08
0.06
0.04
0.02
0.00
Stopping Probability (25mm)
+/- 0.05 %
+/- 0.1 %
+/- 0.2 %
TOF (s)
0.150
0.10
0.05
TOF(s)
0
100
200
300
400
500
Distance from the Be window, z (mm)

(b)

Figure 6

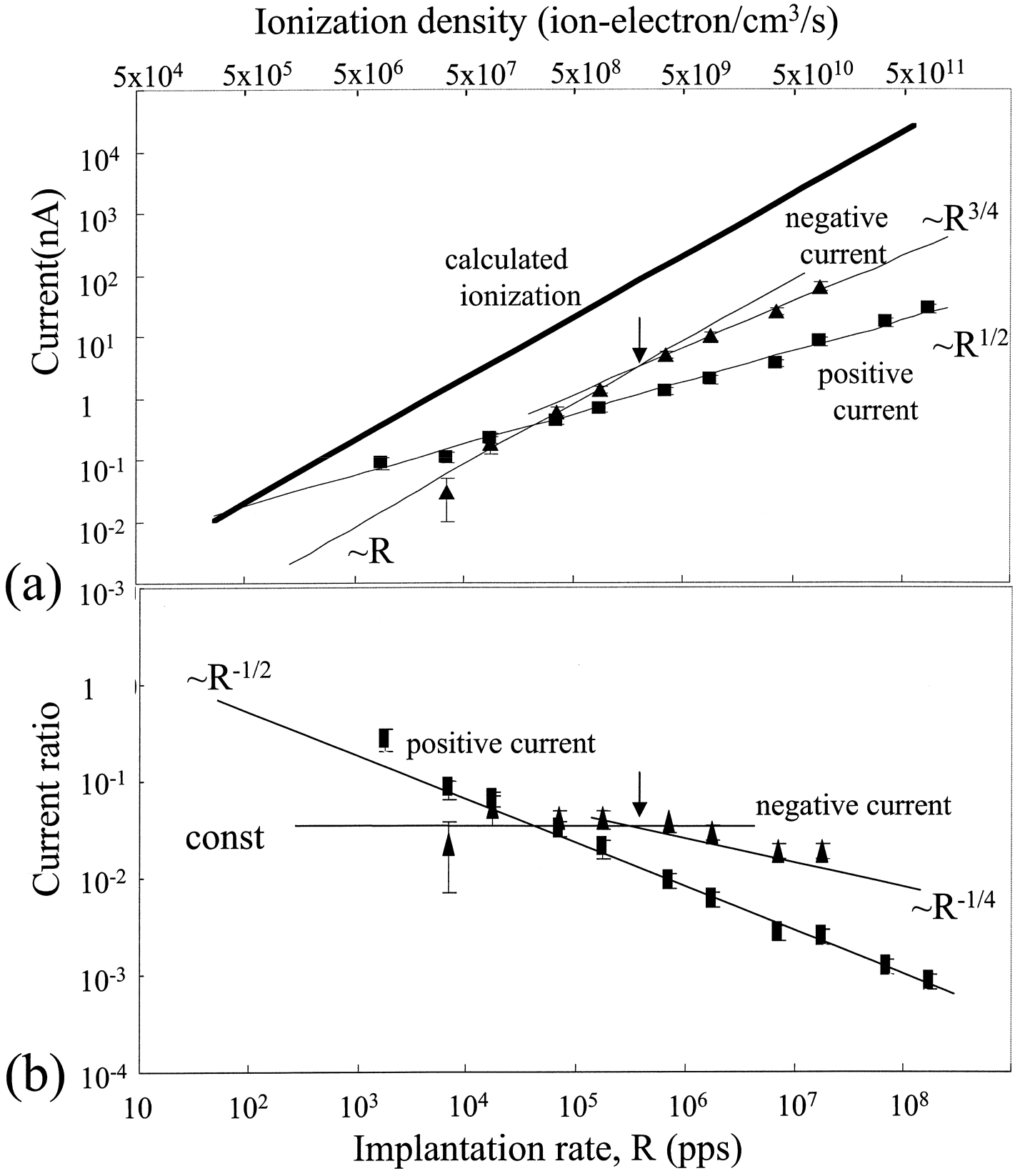
Ionization density (ion-electron/cm3/s)
5x10^4
5x10^5
5x10^6
5x10^7
5x10^8
5x10^9
5x10^10
5x10^11
Current(nA)
10^4
10^3
10^2
10^1
1
10^-1
10^-2
10^-3
calculated ionization
negative current
~R^3/4
~R^1/2
positive current
~R
(a)
Current ratio
1
10^-1
10^-2
10^-3
10^-4
~R^-1/2
positive current
negative current
const
~R^-1/4
(b)
10
10^2
10^3
10^4
10^5
10^6
10^7
10^8
Implantation rate, R (pps)

Figure 7

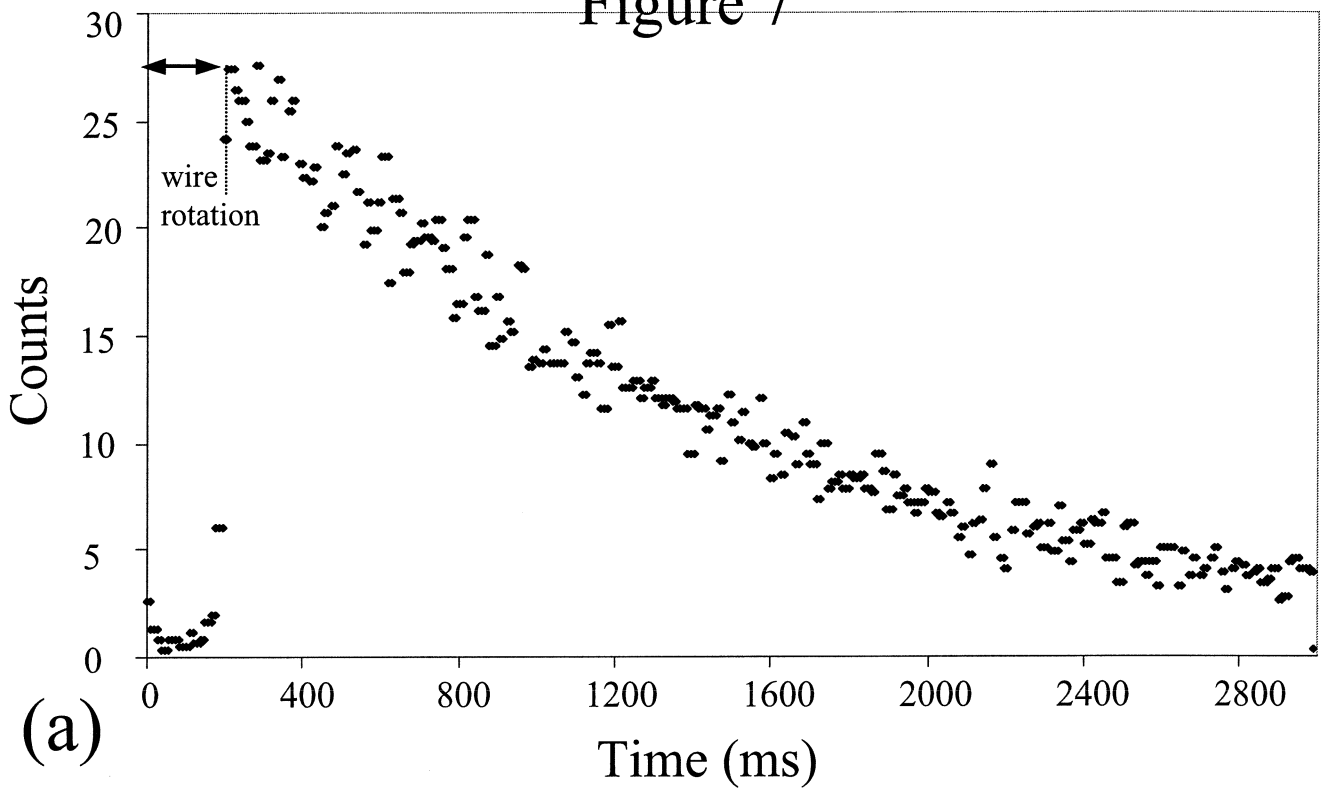
30
25
20
15
10
5
0
Counts
wire
rotation
0
400
800
1200
1600
2000
2400
2800
Time (ms)

(a)

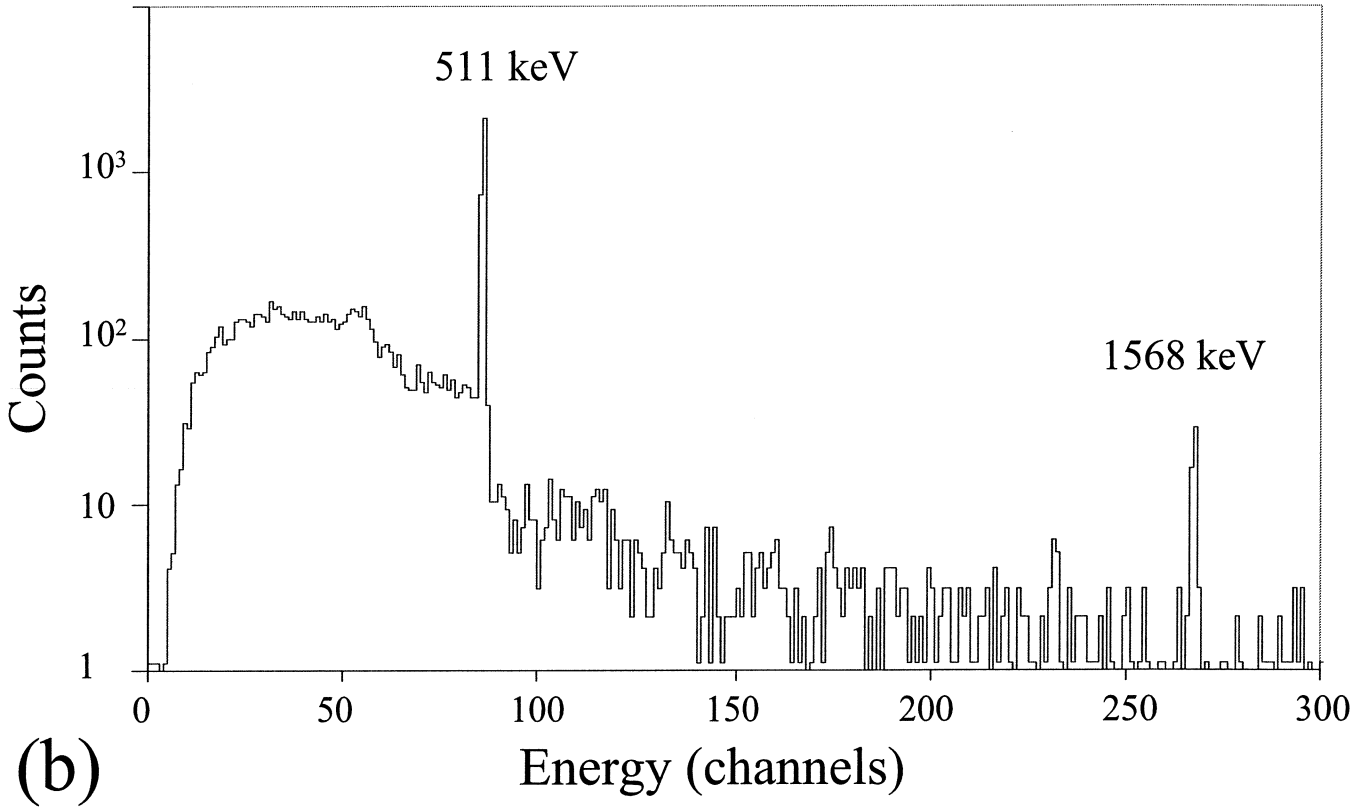
511 keV
1568 keV
10^3
10^2
10
1
Counts
0
50
100
150
200
250
300
Energy (channels)

(b)

Figure 8

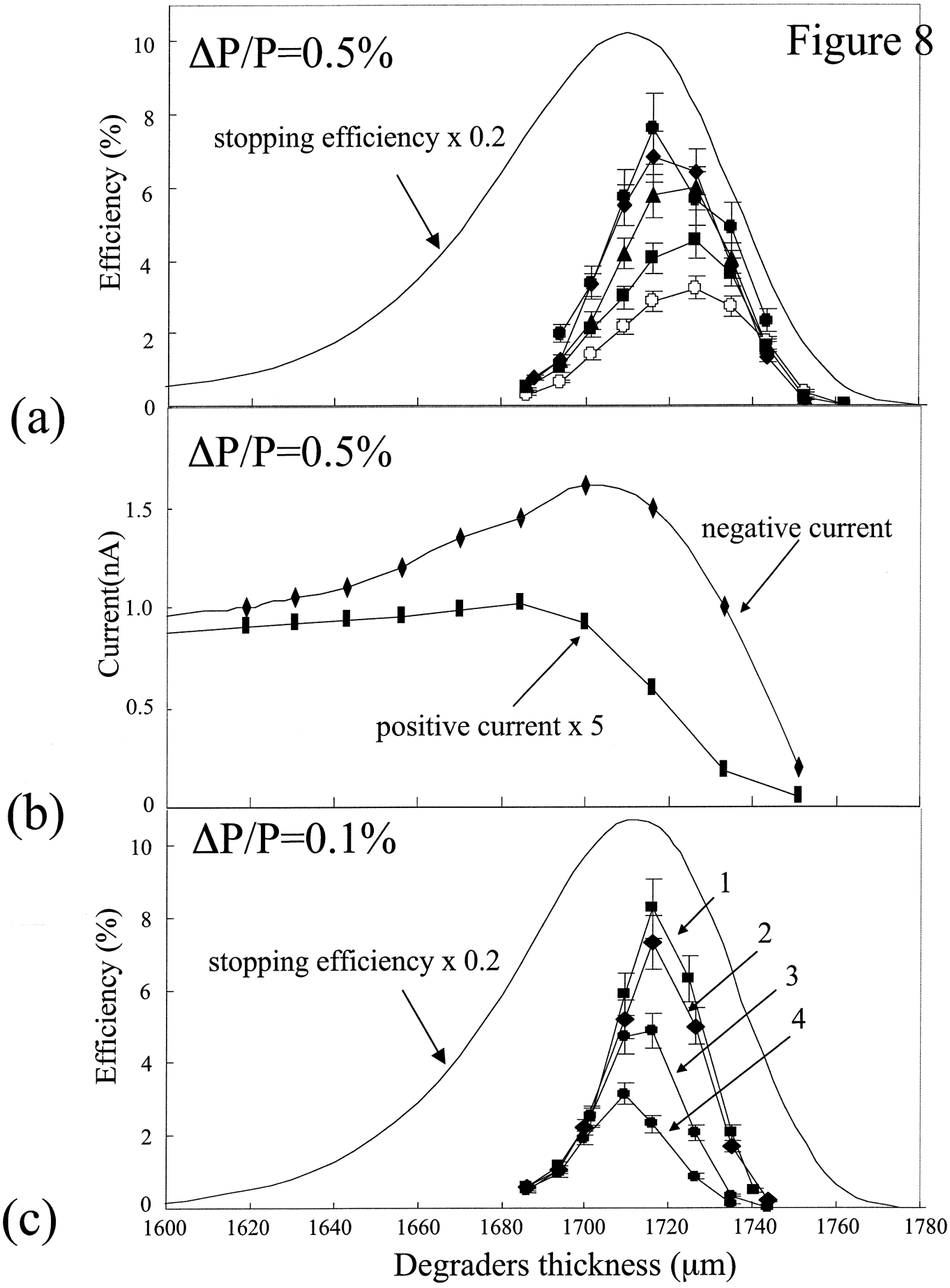
(a)
ΔP/P=0.5%
stopping efficiency x 0.2
Efficiency (%)
0
2
4
6
8
10
(b)
ΔP/P=0.5%
negative current
positive current x 5
Current(nA)
0
0.5
1.0
1.5
(c)
ΔP/P=0.1%
stopping efficiency x 0.2
1
2
3
4
Efficiency (%)
0
2
4
6
8
10
1600
1620
1640
1660
1680
1700
1720
1740
1760
1780
Degraders thickness (μm)

Figure 9

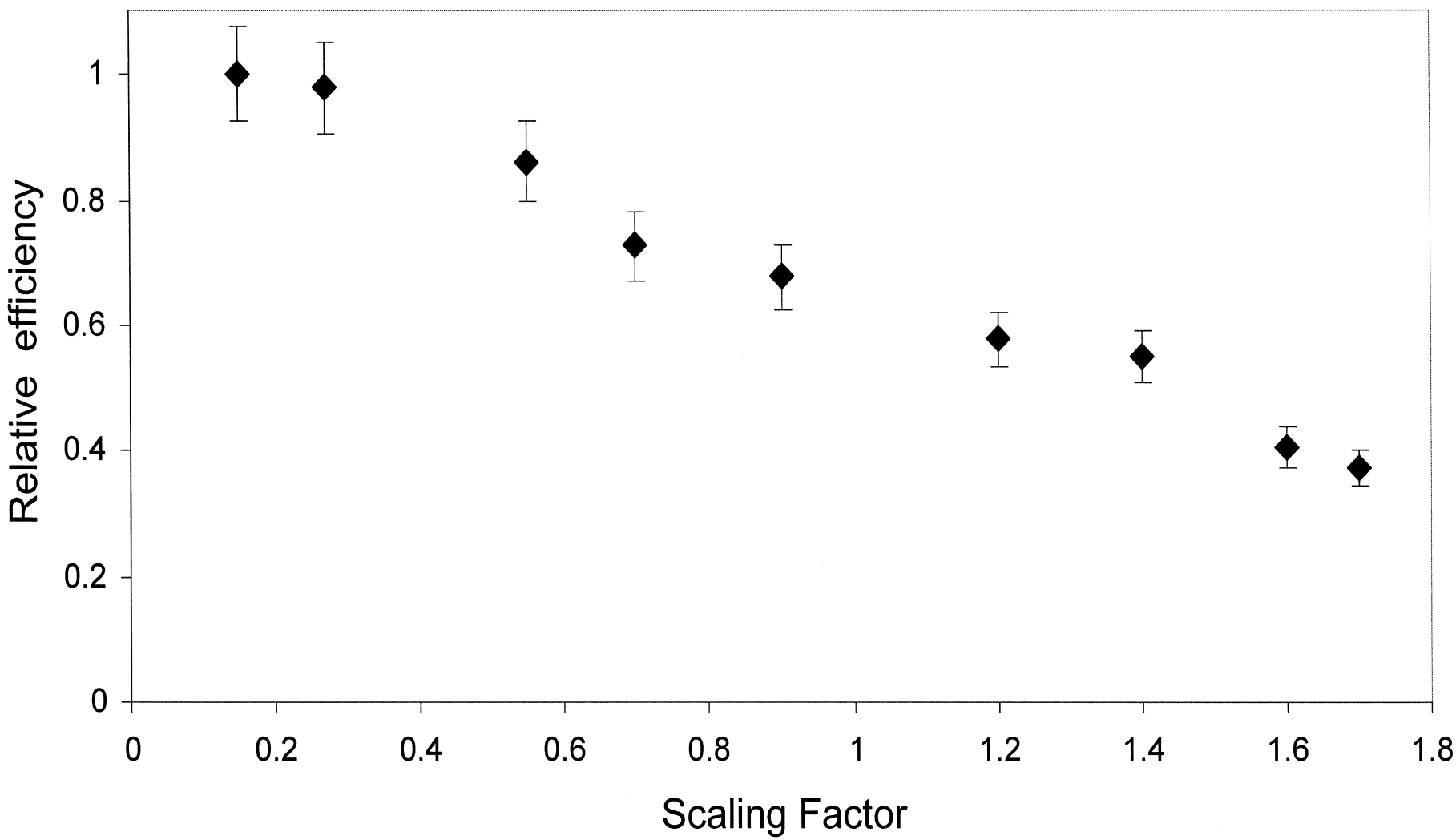
Relative efficiency
0
0.2
0.4
0.6
0.8
1
0
0.2
0.4
0.6
0.8
1
1.2
1.4
1.6
1.8
Scaling Factor

Figure 10

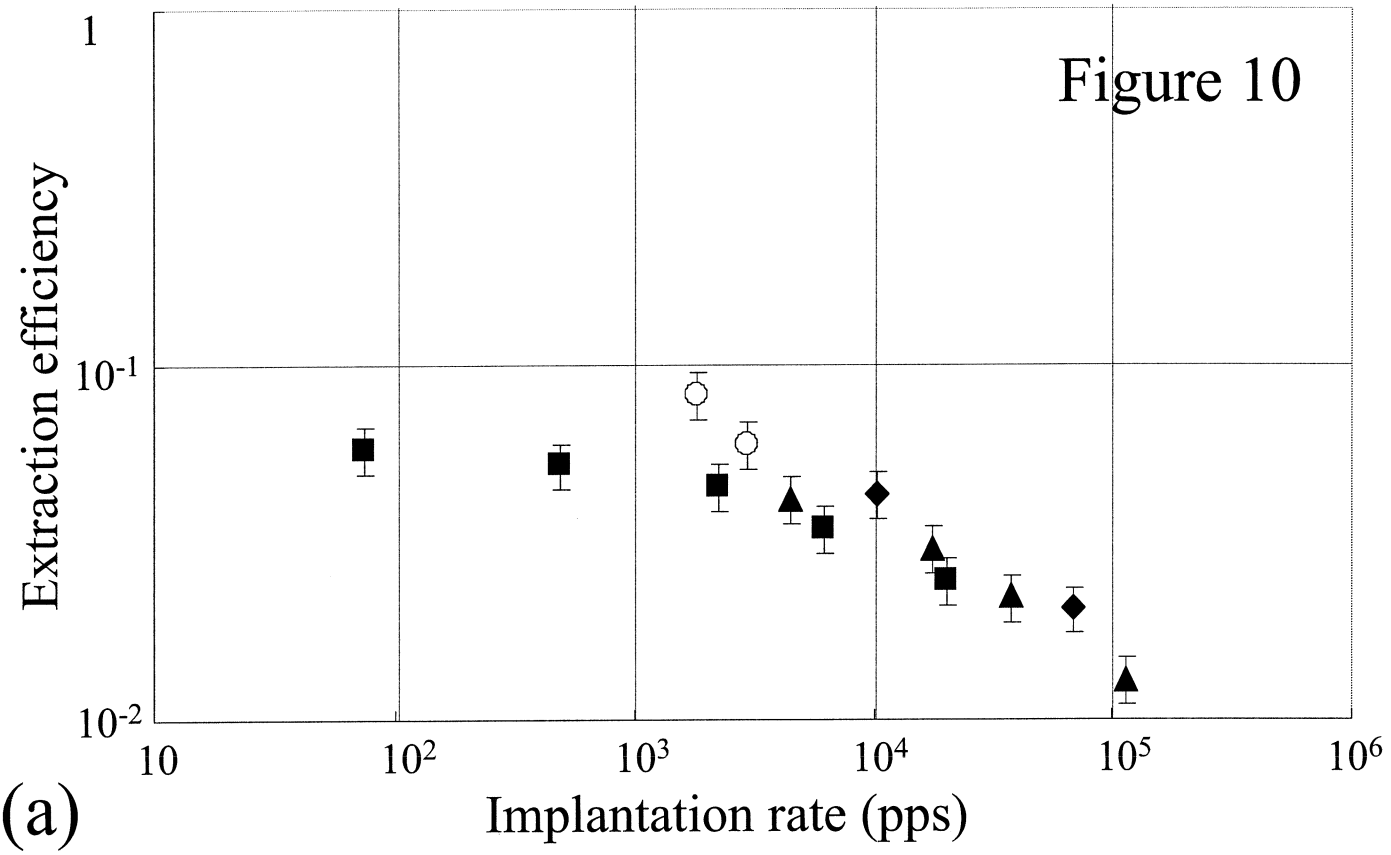
1
10^{-1}
10^{-2}
Extraction efficiency
10
10^2
10^3
10^4
10^5
10^6
Implantation rate (pps)

(a)

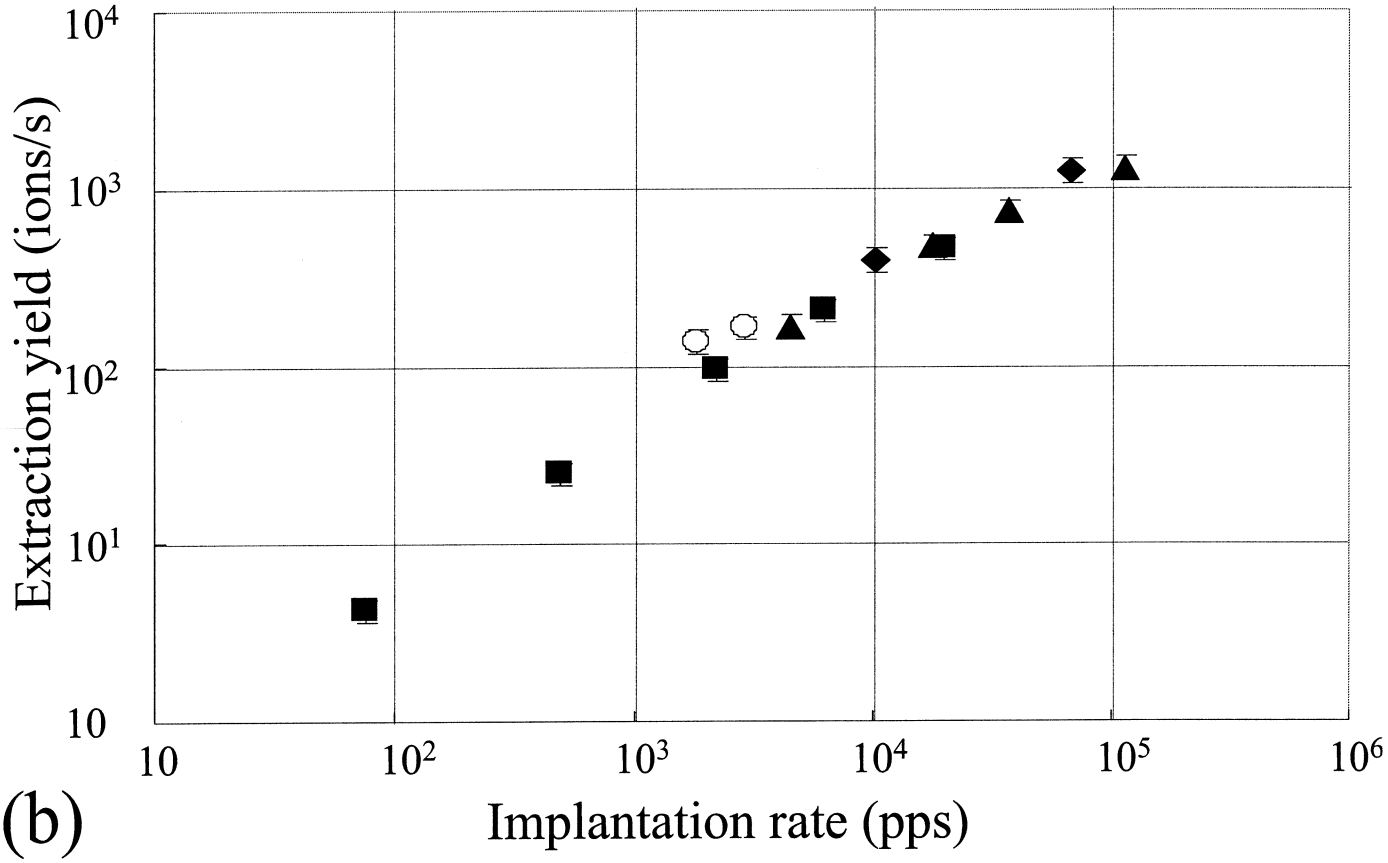
10^4
10^3
10^2
10^1
10
Extraction yield (ions/s)
10
10^2
10^3
10^4
10^5
10^6
Implantation rate (pps)

(b)